SSRG International Journal of Electrical and Electronics Engineering
ISSN: 2348-8379/ https://doi.org/10.14445/23488379/IJEEE-V13I11P106

Volume 13 Issue 11, 89-106, November 2026
© 2026 Seventh Sense Research Group®

Original Article

Pairwise Overlapping State-Lifted LQI Control for a Four-Area Interconnected Load-Frequency Control System

Duy-Thuan Vu[1], Ngoc-Khoat Nguyen[1*], Tung-Linh Nguyen[1], Quoc-Dung Le[1], Anh-Hoa Nguyen[1], Minh-Tuan Le[2]

[1]*Faculty of Automation, Artificial Intelligence and Intelligent Systems, Electric Power University, Hanoi, Vietnam.*
[2]*Faculty of Technology and Engineering, Trade Union University, Hanoi, Vietnam.*

[*]*Corresponding Author: khoatnn@epu.edu.vn*

Received: 04 September 2026 Revised: 30 October 2026 Accepted: 05 November 2026 Published: 25 November 2026

Abstract *- This paper proposes a pairwise overlapping Linear-Quadratic-Integral (LQI) scheme for Automatic Generation Control (AGC), also termed Load-Frequency Control (LFC), of a four-area interconnected power system. Unlike the equal-weight contraction of classical overlapping designs, the method keeps each independent tie-line state inside a nine-state pair model, treats the remaining tie-line flows as signed boundary inputs and fuses duplicated commands with explicit convex weights. A full-column-rank lifting map and its Moore-Penrose left inverse keep the 27-dimensional design space consistent with the 19-state physical model. The resulting feedback matrix uses only neighboring-area information and contains 46 nonzero coefficients, compared with 76 for centralized LQI. Exponential stability is certified numerically by a pairwise block-diagonal Lyapunov function, and a robust linear matrix inequality guarantees quadratic stability for independent coefficient variations of up to ±39%. Classical PI, decentralized LQI, a structured-optimal LQI with the same sparsity pattern and centralized LQI are compared for a single load step, sequential multi-area load changes and a coordinated parameter variation. Relative to PI, the overlapping controller reduces the peak frequency deviation by 61.5%-67.8% and the frequency IAE by 83.6%-85.9%; its peak frequency deviation exceeds that of centralized LQI by 1.6%-2.6%, while 55.6% fewer remote signals are exchanged. The design tolerates communication delays of up to 4 s, but its weights must be retuned when generation-rate constraints are active. These results show that a nearest-neighbor pattern fixed by the tie-line graph recovers most of the centralized performance.*

Keywords *- Automatic Generation Control (AGC), Decentralized control, Inclusion principle, Linear Quadratic Integral control, Sparse feedback.*

1. Introduction

Automatic Generation Control (AGC), also termed Load-Frequency Control (LFC), is the secondary control layer of interconnected power systems that restores area frequencies and scheduled tie-line interchanges after an active-power imbalance [1-3]. Conventional PI control is attractive because of its simplicity, whereas centralized optimal control, introduced for LFC as early as [4], exploits a full state model but requires information from the whole system [5]. As the number of control areas grows, the associated communication and coordination burden motivates sparse, decentralized and distributed feedback structures [6-15].

In overlapping control, local controllers are designed for subsystems that share interface states by means of expansion and contraction mappings between the physical and the lifted state spaces [16, 17]. Its application to LFC is established [18-20], and the choice of the overlapping subsystems has also been studied [21]. In the overlapping LQ designs of Chen and Stanković for multi-area AGC [18, 20], the subsystems are expanded through the inclusion principle and the contracted law is obtained from the expansion-contraction pair. The present work addresses a narrower question, and its mathematical differences from these designs are listed at the end of this section: how to define a fully specified pairwise lifting for a four-area chain that keeps only three independent tie-line states, how to combine duplicated interface commands, and how to evaluate the resulting fixed sparse feedback on the feasible lifted subspace.

The issue has practical weight because synchronous machines are increasingly being replaced by renewable generation. The time window available to secondary control to arrest a frequency excursion is becoming smaller, and the volatility of net demand that AGC/LFC loops are asked to track is growing [11-13]. Moreover, system operators prefer not to rely on wide-area communication for routine regulation, both because of latency and packet loss and because a single

 This is an open access article under the CC BY-NC-ND license (http://creativecommons.org/licenses/by-nc-nd/4.0/)

communication fault should not destabilize more than a small neighborhood of the network [19, 22, 23]. These two pressures point to the same requirement: feedback laws that approach the performance of a fully centralized design while needing only a bounded, physically interpretable pattern of information exchange.

An alternative route to the same objective is to approach the problem from the perspective of optimization instead of structural decomposition, where sparsity is treated as an explicit design objective, and the feedback pattern and the feedback gains are computed simultaneously [24-26]. Such sparsity-promoting formulations let the optimization select the links that matter, but the resulting architecture is not fixed a priori and can be difficult to justify to a system operator who expects the feedback structure to mirror the physical tie-line topology.

In contrast, the overlapping-decomposition approach used here prescribes a communication pattern a priori, based on the tie-line graph, to determine which states each local controller may observe. The open question is then whether this two-step design, local synthesis followed by convex fusion, recovers most of the performance of a centralized law.

The literature reviewed in Section 2 leaves three gaps. First, overlapping AGC/LFC designs [18-20] establish the inclusion principle and the associated stability conditions, but the complete lifting, contraction and command-fusion maps are seldom given in a directly reproducible form, in particular when the tie-line states must remain independent, and the duplicated commands are commonly merged by equal-weight averaging without examining how the fusion weights affect stability and performance. Second, decentralized and distributed LQR-type schemes [7, 27, 28] impose a sparse gain structure, yet the performance lost with respect to the centralized optimum is rarely quantified with the same disturbances and the same indices. Third, sparsity-promoting methods [24, 25] reduce the number of communication links, but the resulting feedback pattern depends on the weights and is not known before tuning. Fourth, structured designs are rarely compared with the best gain that has the same sparsity pattern, so it remains unclear whether the gap to centralized control is caused by the information pattern itself or by the decomposition-based synthesis. The problem addressed in this paper is therefore to design, for a four-area chain, a secondary controller whose information pattern is fixed a priori by the tie-line graph, whose construction is fully explicit, and whose performance gap from centralized LQI is measured under identical conditions.

To solve this problem, the paper makes four contributions. (i) A pairwise lifting is constructed in which each nine-state pair model retains only its own tie-line state, while the flows of the other tie-lines enter as signed boundary inputs Equations (23)-(39); the lifted space therefore has dimension 27 without duplicated tie-line states, and the selection map V has full column rank with its Moore-Penrose left inverse U as the contraction Equations (40)-(52). (ii) The duplicated commands are fused through convex weights Equations (63)-(67), which contain the equal-weight contraction of the inclusion principle as the special case $\eta_2 = \eta_3 = 0.5$, and the influence of these weights on the stability margin, the quadratic cost and disturbance rejection is quantified. (iii) The stability statements are verified numerically: a block-diagonal pairwise Lyapunov function on $\mathrm{im}(V)$, a robust LMI over an explicit coefficient envelope and an a posteriori cost ratio with respect to centralized LQI are reported. (iv) The controller is benchmarked against classical PI, decentralized LQI, a structured-optimal LQI with the same sparsity pattern and centralized LQI, and its communication load, tolerance to delay and measurement noise, sensitivity to generation-rate constraints and scalability to chains of up to ten areas are assessed.

The remainder of the paper is organized as follows. Section 2 reviews related work and positions the present study. Section 3 describes the four-area model, and Section 4 introduces the pairwise state lifting. Controller synthesis and command fusion are presented in Section 5, and the stability and performance statements in Section 6. Simulation results are discussed in Section 7, and Section 8 concludes the paper.

2. Literature Review

2.1. Centralized, Decentralized and Distributed AGC/LFC

Classical approaches to AGC/LFC are based on distributed PI loops acting on the local area control error. This architecture is chosen for operational use due to its simplicity and robustness to model uncertainty [1, 2]. With the increase in interconnections, a significant body of work has examined whether the local loops can be coordinated or replaced by an explicit multivariable design to reduce the frequency and tie-line excursions after a disturbance. Early surveys traced this evolution from tie-line bias control to optimal and adaptive schemes [3], and more recent reviews discuss the additional difficulties introduced by low-inertia, renewable-rich grids [15]. Rasolomampionona et al. review these developments, noting the movement toward hierarchical and distributed structures that maintain local autonomy but permit limited sharing of information between neighboring areas [5].

Distributed formulations based on consensus, optimal or robust-adaptive principles have been proposed for the resulting feedback laws, reporting gains in disturbance rejection over classical PI control at the cost of additional communication and coordination overhead [6-9]. Distributed model predictive control has also been applied to AGC, with neighboring controllers exchanging predicted trajectories in order to approach centralized performance [14]. Hierarchical bi-level schemes combine local correction and inter-area coordination explicitly by assigning fast local correction to an inner loop and slower coordination to an outer one [10].

The robustness to renewable variability and parametric uncertainty has been addressed with metaheuristic PIDF tuning, battery-storage-augmented control and photovoltaic-aware distributed schemes, but each of them targets a particular source of model mismatch rather than a general class of uncertainty [11-13].

Following the optimal-control formulation of the megawatt-frequency problem [4], direct LFC designs have been presented using decentralized LQR and output feedback, generally by pre-assigning a block-diagonal or other sparse gain structure and solving the resulting constrained optimal control problem [23, 27, 28], and robust counterparts formulated as linear matrix inequalities extend this idea to explicit uncertainty and delay margins [22]. Model predictive and fuzzy-logic controllers are further options when actuator constraints or nonlinear characteristics dominate the design [29, 30].

Two observations are common in this literature: a fixed decentralized or block-sparse structure trades some performance for a large reduction in information requirements, and the magnitude of this trade-off is rarely quantified with the same disturbance set and the same performance indices for both the sparse and the centralized design. The present study addresses this gap explicitly.

2.2. Overlapping Decomposition and Sparsity-Promoting Control

Overlapping decomposition looks at the same trade-off from a different angle. Instead of partitioning the state vector into disjoint blocks, Ikeda, Šiljak and White proposed to expand the state vector into an over-complete lifted space in which interconnected subsystems share their interface states, so that each local controller can be designed as if it owned the full dynamics of its immediate neighborhood [16, 17].

A contraction mapping then projects the lifted design back to the physical state space, and the stability of the assembled closed loop is certified by the residual coupling left over from this projection. Chen and Stanković generalized this framework to multi-overlapping (possibly nested) structures and applied it to the AGC of multi-area power systems, where the overlapping information pattern is naturally related to the tie-line graph of an interconnected grid [18, 20].

Subsequent work included output feedback and robustness margins in the overlapping AGC design [19], and more recent work has addressed the question of how a large-scale system should be decomposed into overlapping subsystems in the first place, treating the choice of subsystem boundaries as a design variable rather than a fixed input [21]. The sparsity-promoting line of research formulates the search for a sparse feedback structure as a convex optimization problem with an $\ell 1$-type penalty that is solved using the alternating direction method of multipliers to balance the closed-loop performance against the number of active feedback links [24]. This approach has been applied to wide-area damping control of power networks with encouraging results [25]. Reviews on decentralized control consider both families, structural decomposition and sparsity optimization, as complementary answers to the same scalability problem [26].

What remains relatively unexplored is a fully worked overlapping design for an interconnected multi-area AGC/LFC system in which the lifting, the contraction and the convex fusion of duplicated commands are stated explicitly enough to be reproduced, and in which the resulting sparse feedback law is benchmarked against both classical PI and centralized LQI control under an identical set of disturbances and performance indices.

2.3. Research Gap and Positioning of the Present Study

Table 1 compares the present study with representative structured AGC/LFC designs. The comparison is qualitative, because the cited works use different test systems, disturbances and performance indices, so that a direct numerical comparison of their reported values would not be meaningful.

For this reason, the quantitative comparison in Section 7 is made against classical PI, decentralized LQI, a structured-optimal LQI with the same sparsity pattern and centralized LQI, all implemented on the same model. The distinguishing features of the present study are an information pattern fixed a priori by the tie-line graph, explicit and reproducible lifting, contraction and fusion maps, and a measured performance-information trade-off with respect to the centralized optimum.

From a critical standpoint, the families in Table 1 differ mainly in the origin of the information pattern and in what is certified for the implemented law. Decentralized LQR and LQI designs [23, 27, 28] need no communication, but they react to a disturbance in a neighboring area only through the local frequency. Distributed MPC [14, 29] exploits neighbor predictions, at the price of an online optimization and iterative data exchange within each sampling period. Sparsity-promoting methods [24, 25] select the links by optimization, so the pattern changes with the weights and may contain links between distant areas. Overlapping designs [18-20] fix the pattern through the decomposition, but the contracted law is usually obtained by equal-weight averaging and its stability is inferred from the expanded system.

The gap addressed here is therefore not limited to a clearer presentation of the method; it concerns three quantitative questions: how close a pattern fixed by the tie-line graph comes to the structured optimum for the same pattern and to the centralized optimum, how the fusion weights influence this gap, and which stability and robustness statements can be certified numerically for the contracted law.

Table 1. Comparison of the present study with representative structured AGC/LFC designs

Ref.	Control structure	Design method	Information used online	Pattern fixed a priori
[20]	Overlapping decentralized	Inclusion principle, decentralized state feedback	Overlapping subsystem states	Yes
[19]	Overlapping decentralized	Robust output feedback	Overlapping subsystem outputs	Yes
[7]	Distributed	Distributed LQR	Local and neighboring areas	Yes
[28]	Decentralized	Optimal LQR with decentralized structure	Local area states	Yes
[29]	Distributed	Model predictive control	Local states and neighbor predictions	Yes
[24, 25]	Sparse wide-area	Sparsity-promoting optimal control (ADMM)	Links selected by optimization	No
This study	Pairwise overlapping	Three nine-state LQI problems with convex command fusion	Own and adjacent-area states	Yes (tie-line graph)

3. Four-Area AGC/LFC Model

3.1. Independent Tie-Line States and Component Dynamics

Consider an interconnected power system model with four control areas forming a chain 1-2-3-4 with positive edge orientations 1→2, 2→3, and 3→4. Let $p = \mathrm{col}(\Delta P_{12}, \Delta P_{23}, \Delta P_{34})$. The node-edge incidence matrix is as follows:

$$H = \begin{bmatrix} 1 & 0 & 0 \\ -1 & 1 & 0 \\ 0 & -1 & 1 \\ 0 & 0 & -1 \end{bmatrix} \in \mathbb{R}^{4\times 3} \tag{1}$$

$$h_e \triangleq H(:, e) \tag{2}$$

With $f = \mathrm{col}(\Delta f_1, \Delta f_2, \Delta f_3, \Delta f_4)$, the linearized frequency, governor, turbine, and tie-line equations are as follows:

$$M_i \dot{\Delta f_i} = \Delta P_{t,i} - D_i \Delta f_i - (Hp)_i - \Delta P_{L,i}, i \in \{1,2,3,4\} \tag{3}$$

$$T_{g,i} \dot{\Delta P}_{g,i} = -\Delta P_{g,i} - R_i^{-1} \Delta f_i + u_i. \tag{4}$$

$$T_{t,i} \dot{\Delta P}_{t,i} = -\Delta P_{t,i} + \Delta P_{g,i} \tag{5}$$

$$\dot{p}_e = 2\pi T_e h_e^{\mathsf{T}} f, \qquad e \in \{12,23,34\} \tag{6}$$

$$\dot{p} = 2\pi T H^{\mathsf{T}} f \tag{7}$$

In the above equations, M, D, R, Tg, Tt, Bf and T denote positive diagonal matrices.

3.2. ACE Integration and 19-State Realization

Under the tie-line bias control strategy, each area uses an Area-Control Error (ACE), which combines the local frequency deviation with the net tie-line power deviation. The ACE signals and their integrals are defined as follows:

$$\mathrm{ACE} = B_f f + Hp \tag{8}$$

$$B_f = \mathrm{diag}(B_1, B_2, B_3, B_4) \succ 0 \tag{9}$$

$$\dot{\xi} = \mathrm{ACE} = B_f f + Hp \tag{10}$$

$$\xi = [\xi_1 \quad \xi_2 \quad \xi_3 \quad \xi_4]^{\mathsf{T}} \tag{11}$$

$$x = \mathrm{col}\big(f, P_g, P_t, p\big) \in \mathbb{R}^{15} \tag{12}$$

$$z = \mathrm{col}(x, \xi) \in \mathbb{R}^{19} \tag{13}$$

$$\dot{z} = A_a z + B_a u + E_a d \tag{14}$$

$$d \equiv P_L \in \mathbb{R}^4 \tag{15}$$

The augmented state is $z = \mathrm{col}(f, P_g, P_t, p, \xi) \in \mathbb{R}^{19}$. The compact realization and its matrices are

$$A_a = \begin{bmatrix} -M^{-1}D & 0 & M^{-1} & -M^{-1}H & 0 \\ -T_g^{-1}R^{-1} & -T_g^{-1} & 0 & 0 & 0 \\ 0 & T_t^{-1} & -T_t^{-1} & 0 & 0 \\ 2\pi T H^{\mathsf{T}} & 0 & 0 & 0 & 0 \\ B_f & 0 & 0 & H & 0 \end{bmatrix} \in \mathbb{R}^{19\times 19} \tag{16}$$

$$B_a = \mathrm{col}\big(0, T_g^{-1}, 0,0,0\big) \in \mathbb{R}^{19\times 4} \tag{17}$$

$$E_a = \mathrm{col}(-M^{-1}, 0,0,0,0) \in \mathbb{R}^{19\times 4} \tag{18}$$

The aim of AGC/LFC is to drive the frequency and tie-line power deviations to zero, or at least within acceptable tolerances, so that zero steady-state error is the ideal objective.

The analysis assumes a fixed connected topology, positive finite plant parameters, sufficient generation reserve, full synchronized state availability, ideal neighboring communication, and operation outside sustained actuator saturation. The nominal parameters of the test system are listed in Table 2.

Table 2. Nominal parameters of the four-area test system

Parameter	Area 1	Area 2	Area 3	Area 4
M (p.u.·s/Hz)	0.1667	0.2222	0.1600	0.1304
D (p.u./Hz)	0.008333	0.008889	0.008000	0.008696
R (Hz/p.u.)	2.4	2.7	2.5	2.0
Tg (s)	0.080	0.072	0.070	0.085
Tt (s)	0.300	0.330	0.350	0.375
B (p.u./Hz)	0.425	0.425	0.425	0.425

4. Pairwise Overlapping State Lifting

4.1. Pair Models and Boundary Coupling

For edge $k = (i, j)$, each pair state contains the four local states of both incident areas and their internal tie-line state. External-edge contributions are treated as signed boundary coupling rather than deleted physical states:

$$\chi_{ij} = \text{col}(\Delta f_i, \Delta P_{g,i}, \Delta P_{t,i}, \Delta f_j, \Delta P_{g,j}, \quad \Delta P_{t,j}, p_{ij}, \xi_i, \xi_j) \in \mathbb{R}^9 \quad (19)$$

$$u_{ij} = \begin{bmatrix} u_i^{(ij)} & u_j^{(ij)} \end{bmatrix}^{\mathsf{T}} \quad (20)$$

$$d_{ij} = [\Delta P_{L,i} \quad \Delta P_{L,j}]^{\mathsf{T}} \quad (21)$$

$$q_{ij} = \begin{bmatrix} q_i^{(ij)} & q_j^{(ij)} \end{bmatrix}^{\mathsf{T}} \quad (22)$$

$$\dot{\chi}_{ij} = A_{ij}\chi_{ij} + B_{ij}u_{ij} + E_{ij}d_{ij} + G_{ij}q_{ij} \quad (23)$$

$$M_i\dot{f}_i = P_{t,i} - D_i f_i - \sigma_i p_{ij} - q_i^{(ij)} - P_{L,i} \quad (24)$$

$$T_{g,i}\dot{P}_{g,i} = -P_{g,i} - R_i^{-1} f_i + u_i^{(ij)} \quad (25)$$

$$T_{t,i}\dot{P}_{t,i} = -P_{t,i} + P_{g,i} \quad (26)$$

$$\dot{\xi}_i = B_i f_i + \sigma_i p_{ij} + q_i^{(ij)} \quad (27)$$

$$\dot{p}_{ij} = 2\pi T_{ij}\left(f_i - f_j\right) \quad (28)$$

$$M_j\dot{f}_j = P_{t,j} - D_j f_j - \sigma_j p_{ij} - q_j^{(ij)} - P_{L,j} \quad (29)$$

$$T_{g,j}\dot{P}_{g,j} = -P_{g,j} - R_j^{-1} f_j + u_j^{(ij)} \quad (30)$$

$$T_{t,j}\dot{P}_{t,j} = -P_{t,j} + P_{g,j} \quad (31)$$

$$\dot{\xi}_j = B_j f_j + \sigma_j p_{ij} + q_j^{(ij)} \quad (32)$$

$$\sigma_i = +1, \ \sigma_j = -1 \quad (33)$$

$$q^{(12)} = \text{col}(0, p_{23}) \quad (34)$$

$$q^{(23)} = \text{col}(-p_{12}, p_{34}) \quad (35)$$

$$q^{(34)} = \text{col}(-p_{23}, 0) \quad (36)$$

$$B_{ij} = \begin{bmatrix} T_{g,i}^{-1}e_2 & T_{g,j}^{-1}e_5 \end{bmatrix} \quad (37)$$

$$E_{ij} = \begin{bmatrix} -M_i^{-1}e_1 & -M_j^{-1}e_4 \end{bmatrix} \quad (38)$$

$$G_{ij} = \begin{bmatrix} -M_i^{-1}e_1 + e_8 & -M_j^{-1}e_4 + e_9 \end{bmatrix}, e_r \in \mathbb{R}^9 \quad (39)$$

Reinserting the omitted boundary-flow terms, this construction reproduces the corresponding rows of the global model. The local Riccati equations use the nominal pair dynamics, while the assembled stability analysis preserves the residual physical and duplication couplings.

For numerical implementation, the pair state is kept in the equivalent order χij = col(Δfi, ΔPg,i, ΔPt,i, ξi, Δfj, ΔPg,j, ΔPt,j, ξj, pij). This order is used for the Qp entries in Table 3, for the index sets listed in the Appendix and in the simulation code, whereas Equations (43)-(46) lists the same indices in the order of Equation (19).

4.2. Selection, Lifting and Contraction Maps

Let S12, S23, and S34 select the ordered pair states from z. Their row-index lists make the implementation unambiguous:

$$\chi_{12} = S_{12}z \quad (40)$$

$$\chi_{23} = S_{23}z \quad (41)$$

$$\chi_{34} = S_{34}z \quad (42)$$

$$\mathcal{J}_{12} = (1,5,9,2,6,10,13,16,17) \quad (43)$$

$$\mathcal{J}_{23} = (2,6,10,3,7,11,14,17,18) \quad (44)$$

$$\mathcal{J}_{34} = (3,7,11,4,8,12,15,18,19) \quad (45)$$

$$S_k = I_{19}[\mathcal{J}_k, :] \quad (46)$$

$$\tilde{z} \equiv z_e = \mathrm{col}(\chi_{12}, \chi_{23}, \chi_{34}) = Vz \quad (47)$$

$$V = \mathrm{col}(S_{12}, S_{23}, S_{34}) \in \mathbb{R}^{27\times 19} \quad (48)$$

$$U = (V^{\mathrm{T}}V)^{-1}V^{\mathrm{T}} \in \mathbb{R}^{19\times 27} \quad (49)$$

$$UV = I_{19} \quad (50)$$

$$\Pi = VU,\ \Pi^{\mathrm{T}} = \Pi,\ \Pi^2 = \Pi \quad (51)$$

$$\mathcal{V} \triangleq \mathrm{im}(V) = \{\tilde{z}: \Pi\tilde{z} = \tilde{z}\} \quad (52)$$

As V is built by stacking coordinate-selection matrices and all physical states are kept, its columns are linearly independent and $\mathrm{rank}(V) = 19$. Hence, V^TV is invertible and $U = (V^{\mathrm{T}}V)^{-1}V^{\mathrm{T}}$ is a left inverse with $UV = I_{19}$, which allows the physical state to be recovered from any consistent lifted state. The projector $\Pi = VU$ is symmetric and idempotent; hence, it is the orthogonal projector onto the feasible lifted subspace $\mathrm{Im}(V)$, in which duplicated states remain mutually consistent. For any physical closed-loop matrix A_{cl}, the expanded matrix $A_{\mathrm{e}} = VA_{\mathrm{cl}}U$ satisfies $A_eV = VA_{\mathrm{cl}}$. Thus, if $\tilde{z}(0) = Vz(0)$, then $\tilde{z}(\mathrm{t}) = Vz(\mathrm{t})$ for all t, implying that the physical and lifted dynamics are exactly equivalent on $\mathrm{Im}(V)$.

Figure 1 shows the resulting pairwise overlapping LQI architecture and the nearest-neighbor information exchange.

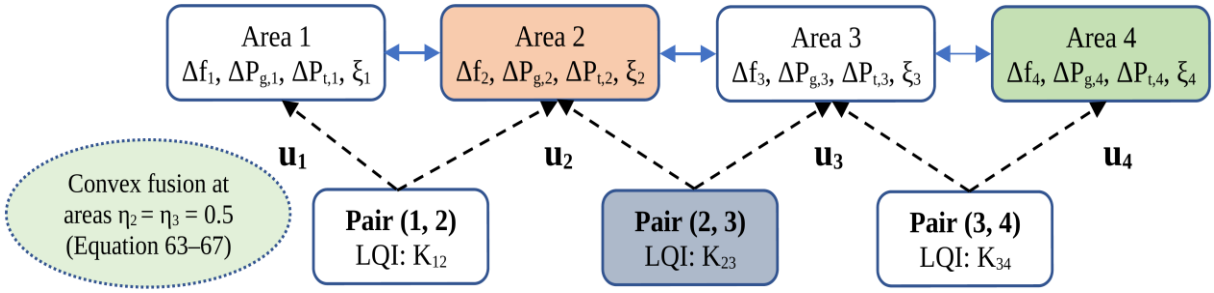

Fig. 1 Pairwise overlapping LQI architecture and Nearest-Neighbor information exchange

5. Controller Synthesis and Fusion

5.1. Centralized and Pairwise LQI Designs

The centralized LQI benchmark minimizes the quadratic criterion in Equation (53) over the augmented 19-state model in Equations (14) and (15), and its gain follows from the Continuous-Time Algebraic Riccati Equation (CARE) in Equation (54) [4, 31]:

$$J_c = \int_0^\infty (z^{\mathrm{T}}Q_c z + u^{\mathrm{T}}R_c u)\ \mathrm{d}t, Q_c \succcurlyeq 0, R_c \succ 0 \quad (53)$$

$$A_a^{\mathrm{T}}P_c + P_cA_a - P_cB_aR_c^{-1}B_a^{\mathrm{T}}P_c + Q_c = 0 \quad (54)$$

$$K_c = R_c^{-1}B_a^{\mathrm{T}}P_c \quad (55)$$

$$u_c = -K_c z \quad (56)$$

For each pair $k \in \{12, 23, 34\}$, the local criterion, CARE, and feedback gain are

$$J_k = \int_0^\infty \left(\chi_k^{\mathrm{T}}Q_k\chi_k + u_k^{\mathrm{T}}R_k u_k\right)\ \mathrm{d}t,$$

$$Q_k \succcurlyeq 0,\ R_k \succ 0 \quad (57)$$

$$A_k^{\mathrm{T}}P_k + P_kA_k - P_kB_kR_k^{-1}B_k^{\mathrm{T}}P_k + Q_k = 0 \quad (58)$$

$$K_k = R_k^{-1}B_k^{\mathrm{T}}P_k \quad (59)$$

$$u_k = -K_k\chi_k \quad (60)$$

$$K_e \equiv K_p = \mathrm{blkdiag}(K_{12}, K_{23}, K_{34}) \in \mathbb{R}^{6\times 27} \quad (61)$$

$$\tilde{u} = -K_p\tilde{z} = -K_pVz \quad (62)$$

5.2. Convex Fusion and Physical Feedback

The duplicated proposals for Areas 2 and 3 are fused with nonnegative weights that sum to one. Symmetric fusion uses $\eta_2 = \eta_3 = 0.5$, as given below:

$$C_u(\eta_2, \eta_3) = \begin{bmatrix} 1 & 0 & 0 & 0 & 0 & 0 \\ 0 & \eta_2 & 1-\eta_2 & 0 & 0 & 0 \\ 0 & 0 & 0 & \eta_3 & 1-\eta_3 & 0 \\ 0 & 0 & 0 & 0 & 0 & 1 \end{bmatrix},$$

$$0 \le \eta_2, \eta_3 \le 1 \quad (63)$$

$$u = C_u\tilde{u} \quad (64)$$

$$\eta_2 = \eta_3 = 1/2 \quad (65)$$

$$K_{\mathrm{ov}} = C_uK_pV \in \mathbb{R}^{4\times 19} \quad (66)$$

$$u = -K_{\mathrm{ov}}z \quad (67)$$

$$\mathcal{J}_1 = \{\chi_{12}\} \quad (68)$$

$$\mathcal{I}_2 = \{\chi_{12}, \chi_{23}\} \quad (69)$$

$$\mathcal{I}_3 = \{\chi_{23}, \chi_{34}\}, \quad \mathcal{I}_4 = \{\chi_{34}\} \quad (70)$$

The resulting law $u = -K_{\mathrm{ov}} z$ uses only local and adjacent-area states. With a numerical threshold of 10-10, its row-wise nonzero counts are (9, 14, 14, 9), totalling 46. This number is both the structural upper bound implied by the pair masks and the numerical count for the reported gains; the centralized gain Kc contains 76 nonzero coefficients. The symmetric choice $\eta_2 = \eta_3 = 0.5$ is adopted for two reasons. The two pair designs that propose a command for an interior area use the same local states and the same tie-line state, so neither proposal is better informed a priori, and equal weights reproduce the pseudo-inverse contraction of the inclusion principle [16, 17], which makes the comparison with classical overlapping designs direct. The influence of other weights is quantified in Section 7.5.

Table 3. Controllers used in all simulations

Controller	Design and fixed settings	Online information
Classical PI	u_i = -0.05 ACE$_i$ - 0.20 ξ_i	Local ACE and integral
Centralized LQI	Q_c: 250 (f), 2 (P_g), 2 (P_t), 80 (p), 350 (ξ); R_c = 0.25 I_4	All 19 states
Overlapping LQI	Q_p = diag(220, 2, 2, 300, 220, 2, 2, 300, 65); R_p = 0.22 I_2	Own and adjacent pair states
Decentralized LQI	Area model (Δf, ΔP_g, ΔP_t, ξ); Q_a = diag(220, 2, 2, 300); R_a = 0.22	Own area states only
Structured-optimal LQI	Sparsity pattern of K_{ov}; minimizes tr(P) with Q_c, R_c; gradient method from K_{ov}	Own and adjacent pair states

The weighting matrices follow the usual AGC priorities. The frequency and integral states receive the largest weights because they define the regulation objectives, the governor and turbine states receive small weights so that the generation response that removes the imbalance is not penalized, and the control weights keep the peak command in all cases below 30% of the 0.20 p.u. limit.

The pair weights R_p and the diagonal of the pair Q matrix were then adjusted so that the overlapping law reaches a closed-loop spectral abscissa of the same order as the centralized design (-0.421 versus -0.503). The two additional benchmarks of Table 3 are described in Section 7.5.

6. Stability and Performance Statement

6.1. Nominal and Residual-Coupling Conditions

After contraction and command fusion, the nominal physical closed loop is

$$A_{\mathrm{cl}} = A_a - B_a K_{\mathrm{ov}} \in \mathbb{R}^{19\times 19} \quad (71)$$

$$\dot{z} = A_{\mathrm{cl}} z \quad (d = 0) \quad (72)$$

For a Hurwitz A_{cl} and any $Q_L \succ 0$, the Lyapunov equation and exponential bound are as follows [32, 33]:

$$A_{\mathrm{cl}}^{\mathsf{T}} P + P A_{\mathrm{cl}} = -Q_L, P \succ 0,\ Q_L \succ 0 \quad (73)$$

$$\| z(t) \|_2 \leq \sqrt{\frac{\lambda_{\max}(P)}{\lambda_{\min}(P)}} \exp\left[-\frac{\lambda_{\min}(Q_L)}{2\lambda_{\max}(P)} t\right] \| z(0) \|_2 \quad (74)$$

To connect local pair stability to the assembled system, define the block-diagonal local closed-loop matrix and the exact residual coupling Δ_c in the lifted space:

$$A_{c,k} = A_k - B_k K_k \quad (75)$$

$$A_{D,c} = \mathrm{blkdiag}\left(A_{c,12}, A_{c,23}, A_{c,34}\right) \quad (76)$$

$$A_e = V A_{\mathrm{cl}} U \quad (77)$$

$$\Delta_c = A_e - A_{D,c} \quad (78)$$

$$A_{c,k}^{\mathsf{T}} P_k + P_k A_{c,k} = -Q_{kL} \quad (79)$$

$$P_D = \mathrm{blkdiag}(P_{12}, P_{23}, P_{34}) \quad (80)$$

$$Q_D = \mathrm{blkdiag}(Q_{12L}, Q_{23L}, Q_{34L}) \quad (81)$$

$$\beta = \lambda_{\min}(Q_D) - 2 \| P_D \Delta_c \|_2 \quad (82)$$

If every local closed-loop matrix is Hurwitz and $\beta = \lambda_{\min}(Q_D) - 2\|P_D\Delta_c\|2 > 0$, the quadratic Lyapunov derivative is strictly negative on $\mathrm{Im}(V)$, which is sufficient for exponential stability of the physical 19-state system:

$$\dot{V}_e = -\tilde{z}^{\mathsf{T}} Q_D \tilde{z} + \tilde{z}^{\mathsf{T}} (\Delta_c^{\mathsf{T}} P_D + P_D \Delta_c) \tilde{z} \quad (83)$$

$$\dot{V}_e \leq -[\lambda_{\min}(Q_D) - 2 \| P_D \Delta_c \|_2] \| \tilde{z} \|_2^2 = -\beta \| \tilde{z} \|_2^2. \quad (84)$$

$$V^{\mathsf{T}} (A_e^{\mathsf{T}} P_D + P_D A_e) V \prec 0 \quad (85)$$

$$P_D = \mathrm{blkdiag}(P_{12}, P_{23}, P_{34}) \succ 0 \quad (86)$$

In this context, the test is sufficient but conservative. If $\beta \leq 0$, it is inconclusive rather than evidence of instability. The projected inequality is used because directions outside $\mathrm{Im}(V)$ do not represent physical trajectories.

For the reported gains, the three local closed-loop matrices are Hurwitz with spectral abscissa -0.496, whereas the physical closed loop has spectral abscissa -0.4208. With $Q_{pkL} = I_9$, the coupling term gives $\|P_D \Delta_c\|_2 = 33.08$ and $\beta = -65.16$, so the norm test is inconclusive. Equations (85) and (86) is a weaker, projected requirement. Solved as an LMI in the three-pair blocks with $P_k \succcurlyeq I_9$, it is feasible, and the largest eigenvalue of $V^T(A_e^T P_D + P_D A_e)V$ equals -270.0. The nominal 19-state closed loop is therefore exponentially stable with a Lyapunov function assembled from pair-level blocks, which is the certificate reported for the contracted law.

6.2. Fixed-Gain Uncertainty and Cost Assessment

For a fixed nominal gain K_{ov}, variations of the physical coefficients can be collected in the norm-bounded factorization $A_{\mathrm{cl}}(\delta) = A_0 + H_\Delta F E_\Delta$, $F^T F \preccurlyeq I$. A quadratic-stability certificate then follows from the standard LMI below [32, 34]:

$$A_{\mathrm{cl}}(\delta) = A_0 + \sum_{r=1}^{q} \delta_r A_r = A_0 + H_\Delta F(\delta) E_\Delta$$

$$|\delta_r| \le 1, \quad F^{\mathsf{T}} F \preccurlyeq I \tag{87}$$

$$\begin{bmatrix} A_0^{\mathsf{T}} P + P A_0 + \varepsilon E_\Delta^{\mathsf{T}} E_\Delta & P H_\Delta \\ H_\Delta^{\mathsf{T}} P & -\varepsilon I_r \end{bmatrix} \prec 0 \tag{88}$$

$$P = P^{\mathsf{T}} \succ 0, \quad \varepsilon > 0 \tag{89}$$

This condition certifies the whole outer uncertainty envelope only when the LMI is solved successfully. In this study, the envelope is constructed from independent variations of ±α on Mi, Di, Ri, Tg,i, Tt,i and Te. The closed-loop matrix is affine in the coefficients 1/Mi, Di/Mi, 1/Tg,i, 1/(Tg,iRi), 1/Tt,i and Te; the interval of each coefficient defines one rank-one term $A_r = h_r e_r^T$ (q = 23), and εI_r in Equations (88) and (89) is replaced by the diagonal multiplier $\mathrm{diag}(\lambda_1, \dots, \lambda_q) \succ 0$, which reduces conservatism. Because the coefficients are bounded independently, the envelope contains every physical combination within ±α.

The resulting bounds are reported in Section 7.6; Case 3 is a single point inside this envelope and is used only to illustrate the time response. The overlapping cost matrix and the worst-case a posteriori ratio with the same Qc and Rc as the centralized design are as follows:

$$A_{\mathrm{cl}}^{\mathsf{T}} P_{\mathrm{ov}} + P_{\mathrm{ov}} A_{\mathrm{cl}} + Q_c + K_{\mathrm{ov}}^{\mathsf{T}} R_c K_{\mathrm{ov}} = 0 \tag{90}$$

$$\rho_J = \lambda_{\max}\left(P_c^{-1/2} P_{\mathrm{ov}} P_c^{-1/2}\right) \tag{91}$$

$$J_c(z_0) \le J_{\mathrm{ov}}(z_0) \le \rho_J J_c(z_0), z_0 \ne 0 \tag{92}$$

The computed value $\rho_J = 1.1788$ is an a posteriori worst-direction bound for the nominal unsaturated linear model. It should not be interpreted as an a priori near-optimality guarantee.

Table 4. Closed-Loop metrics for the three simulation cases (1-ms fixed-step simulation; definitions in Equations (93)-(95))

Case	Controller	max|Δ*f*| (Hz)	max|ΔP_{tie}| (p.u.)	IAE	ITAE	T_s (s)	max|*u*| (p.u.)	$E_{u,T}$
1	Classical PI	0.032508	0.009882	0.177246	1.761374	24.40	0.015000	0.015293
1	Decentralized LQI	0.010755	0.003196	0.032375	0.257990	11.66	0.052612	0.016903
1	Overlapping LQI	0.010461	0.002812	0.029145	0.226703	8.49	0.054908	0.016902
1	Structured-optimal LQI	0.010457	0.002712	0.027830	0.208513	8.91	0.055484	0.016904
1	Centralized LQI	0.010291	0.002652	0.026768	0.200427	8.91	0.056557	0.016916
2	Classical PI	0.025030	0.006266	0.330646	7.057808	19.91	0.012214	0.019296
2	Decentralized LQI	0.009064	0.002510	0.058755	1.236114	7.36	0.044314	0.021301
2	Overlapping LQI	0.008883	0.002341	0.054198	1.128435	7.66	0.045852	0.021300
2	Structured-optimal LQI	0.008900	0.002307	0.053522	1.081209	7.61	0.046139	0.021310
2	Centralized LQI	0.008744	0.002225	0.050176	1.030273	7.56	0.047192	0.021321
3	Classical PI	0.026002	0.007581	0.174341	2.252937	24.67	0.014000	0.014733
3	Decentralized LQI	0.010259	0.002664	0.026310	0.270578	7.69	0.051120	0.016160
3	Overlapping LQI	0.010018	0.002421	0.024533	0.247464	7.48	0.053298	0.016162
3	Structured-optimal LQI	0.009728	0.002053	0.027034	0.271929	8.22	0.055524	0.016194
3	Centralized LQI	0.009762	0.002293	0.023551	0.237654	8.00	0.056055	0.016181

7. Simulation Results and Discussion

7.1. Cases, Limits and Metrics

The nominal model represents four thermal areas without reheat and is not intended to be a calibrated national-grid model, but rather a controller benchmark. The tie-line synchronizing coefficients are $T_{12} = T_{23} = T_{34} = 0.0866$ p.u./rad and the common amplitude limit is $|u_i| \le 0.20$ p.u. The controller gains are computed for the nominal model and then kept constant. All simulations use a fixed-step fourth-order Runge-Kutta integrator with a step of 1 ms, a zero initial state and the amplitude limit applied to every control signal. The CAREs and Lyapunov equations are solved with Schur-based solvers (Python 3.13, NumPy 2.5 and SciPy 1.18), and the LMIs with the interior-point solver Clarabel through

CVXPY 1.9; halving the step changes the reported indices by less than 0.01%. The complete parameter set, the simulation settings and the gain matrices are summarized in the Appendix.The proposed controller is verified in the following three simulation cases:

- Case 1 applies a +0.015 p.u. load step in Area 1 at 5 s (80 s horizon).
- Case 2 applies +0.012 p.u. in Area 2 at 5 s, +0.010 p.u. in Area 4 at 20 s and -0.006 p.u. in Area 1 at 35 s (90 s horizon).
- Case 3 combines a coordinated variation of the plant parameters, given as multipliers of the nominal values, M (1.15, 0.90, 1.10, 0.92); D (1.05, 1.10, 0.95, 1.10); T_g (1.20, 0.90, 1.15, 1.05); T_t (0.90, 1.15, 1.10, 0.95); tie-line coefficients (0.92, 1.08, 0.90), with a +0.014 p.u. load step $\Delta P_{L,3}$ in Area 3 at 8 s; R and B remain nominal.

The performance indices are defined in Equations (93)-(95), where Tf is the simulation horizon. In addition, max|Δf| and max|ΔPtie| are the largest absolute deviations over all areas and all tie-lines, the peak command is $\max_{t,i}|u_i(t)|$, and T_s is the time after the last load event beyond which $\max_i|\Delta f_i(t)| < 1\times10^{-4}$ Hz holds permanently. Because the steady generation increment is non-zero after a step disturbance, the finite-horizon energy depends on the horizon length; it is therefore compared only within the same case and the same time interval. The numerical results of the three scenarios are listed in Table 4.

Figures 2 and 3 present the results of Case 1, Figures 4 and 5 those of Case 2, and Figures 6 and 7 those of Case 3; Figure 8 summarizes the three cases. The curves show the maximum absolute value over the areas, sampled every 10 ms during 12 s after each load event and every 0.1 s elsewhere, with the exact peaks retained, so that the plotted peaks coincide with the values in Table 4.

$$\mathrm{IAE} = \int_0^{T_f} \sum_{i=1}^{4} |\Delta f_i(t)|\,\mathrm{d}t \tag{93}$$

$$\mathrm{ITAE} = \int_0^{T_f} t \sum_{i=1}^{4} |\Delta f_i(t)|\,\mathrm{d}t \tag{94}$$

$$E_{u,T} = \int_0^{T_f} \sum_{i=1}^{4} u_i^2(t)\,\mathrm{d}t \tag{95}$$

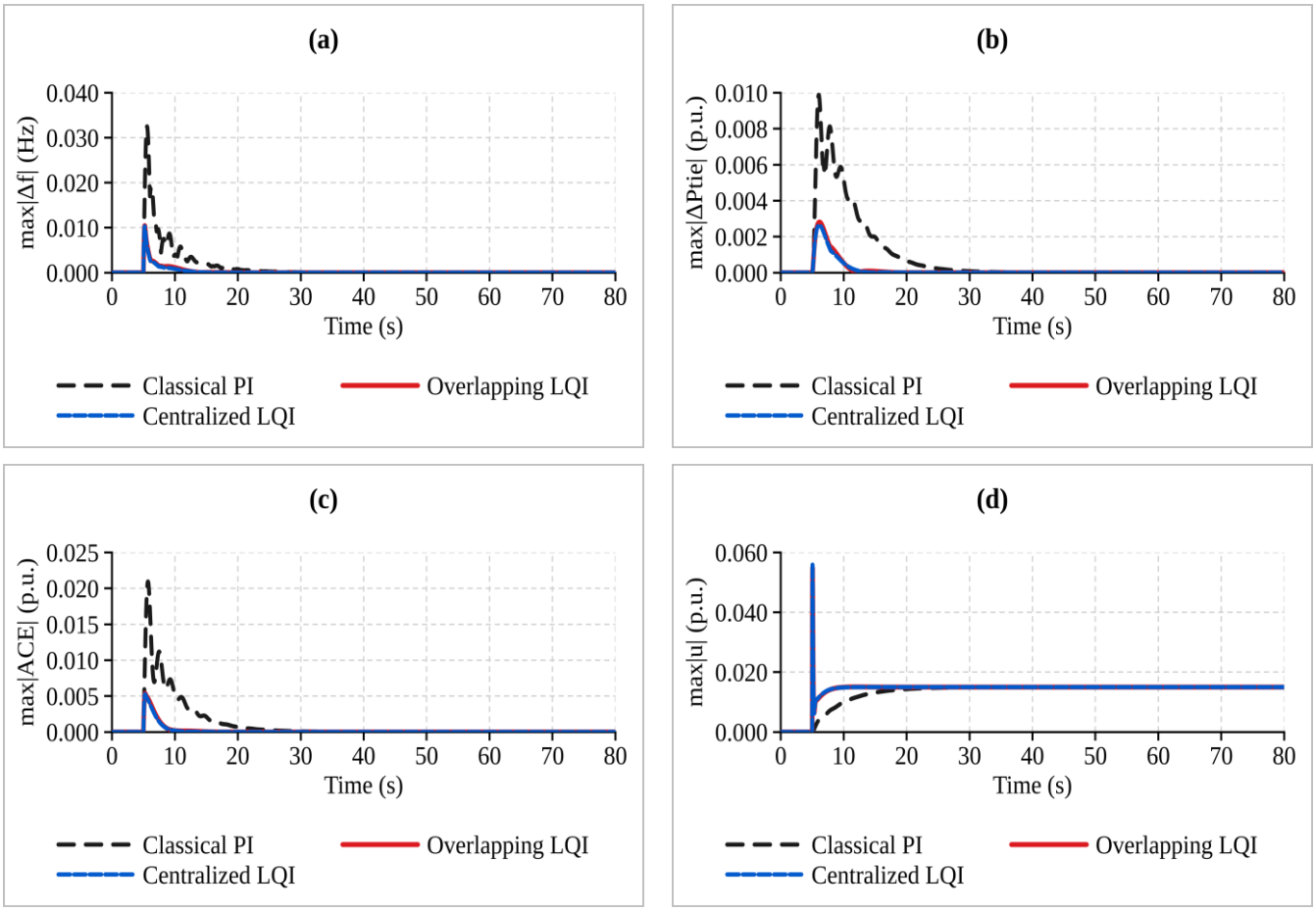

Fig. 2 Comparative responses for case 1 (+0.015 p.u. load in area 1 at 5 s): (a) Maximum absolute frequency deviation, (b) Maximum absolute tie-line power deviation, (c) Maximum absolute ACE, and (d) Maximum absolute AGC command; curves show the maximum absolute value over the areas, with exact peaks retained.

7.2. Case 1: Single Load Step

As shown in Figures 2 and 3, the proposed controller yields max|Δf| = 0.010461 Hz, max|ΔPtie| = 0.002812 p.u., IAE = 0.029145 and Ts = 8.49 s. These values are reduced by 67.82%, 71.54%, 83.56% and 65.21%, respectively, with respect to PI. Compared with the centralized LQI, the overlapping design yields a 1.65% higher frequency peak, an 8.88% higher IAE and a 4.69% shorter settling time. Its peak command, 0.054908 p.u., occurs 51 ms after the load step, remains below both the imposed limit and the centralized value (0.056557 p.u.) and is visible in Figure 2(d). Thus, the sparse design is close to the centralized performance but not uniformly better than it.

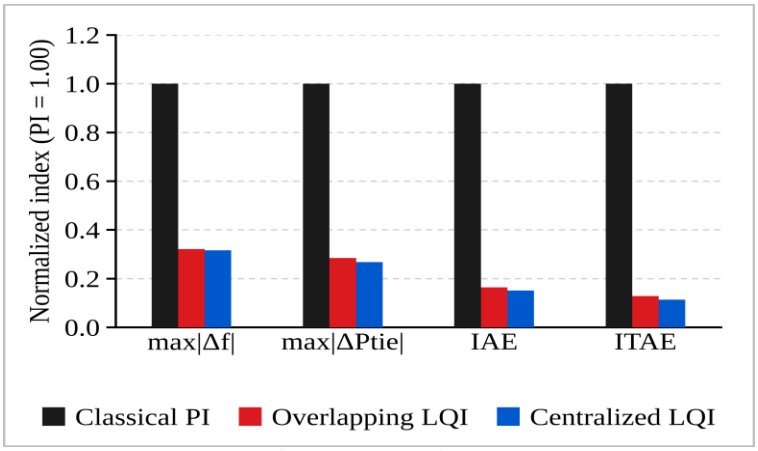

Fig. 3 PI-Normalized performance indices for case 1 (Classical PI = 1.00)

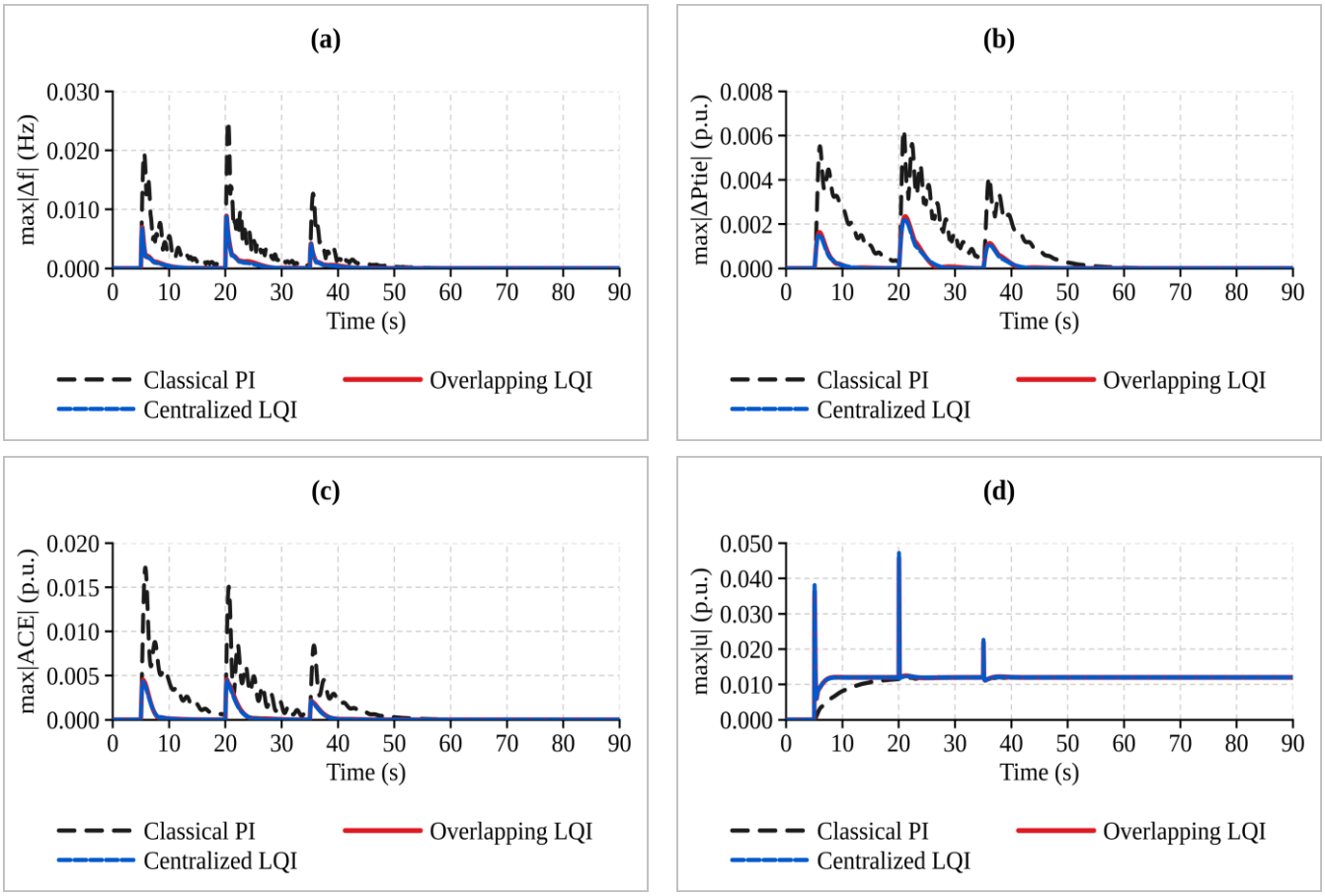

Fig. 4 Comparative responses for case 2 with three sequential load changes: (a) Maximum absolute frequency deviation, (b) Maximum absolute tie-line power deviation, (c) Maximum absolute ACE, and (d) Maximum absolute AGC command; curves show the maximum absolute value over the areas, with exact peaks retained.

7.3. Case 2: Sequential Multi-Area Disturbances

Following each of the three load changes, the overlapping controller brings the frequency, ACE and tie-line deviations back to a neighborhood of zero. The max|Δf|, IAE, ITAE and settling time are 0.008883 Hz, 0.054198, 1.128435 and 7.66 s, respectively. Compared with the PI regulator, the proposed strategy reduces the peak frequency, peak tie-line power, IAE and ITAE by 64.51%, 62.65%, 83.61% and 84.01%, respectively. The peak frequency, IAE and ITAE are 1.59%, 8.02% and 9.53% higher than those of the centralized LQI (see Figures 4 and 5). No controller reaches the common amplitude limit.

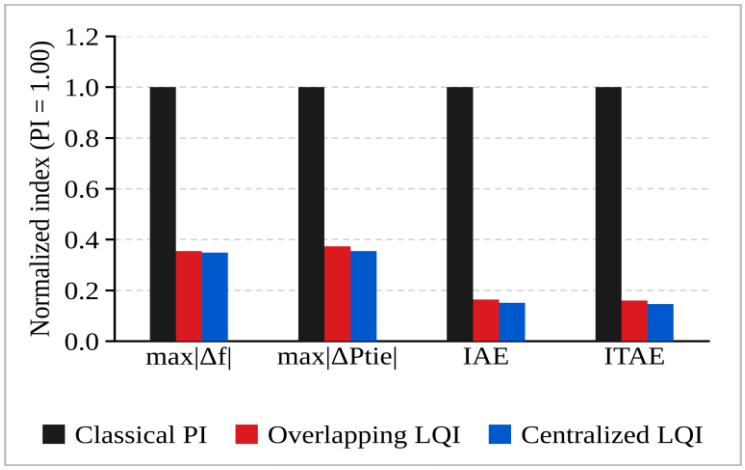

Fig. 5 PI-Normalized performance indices for Case 2 (Classical PI = 1.00)

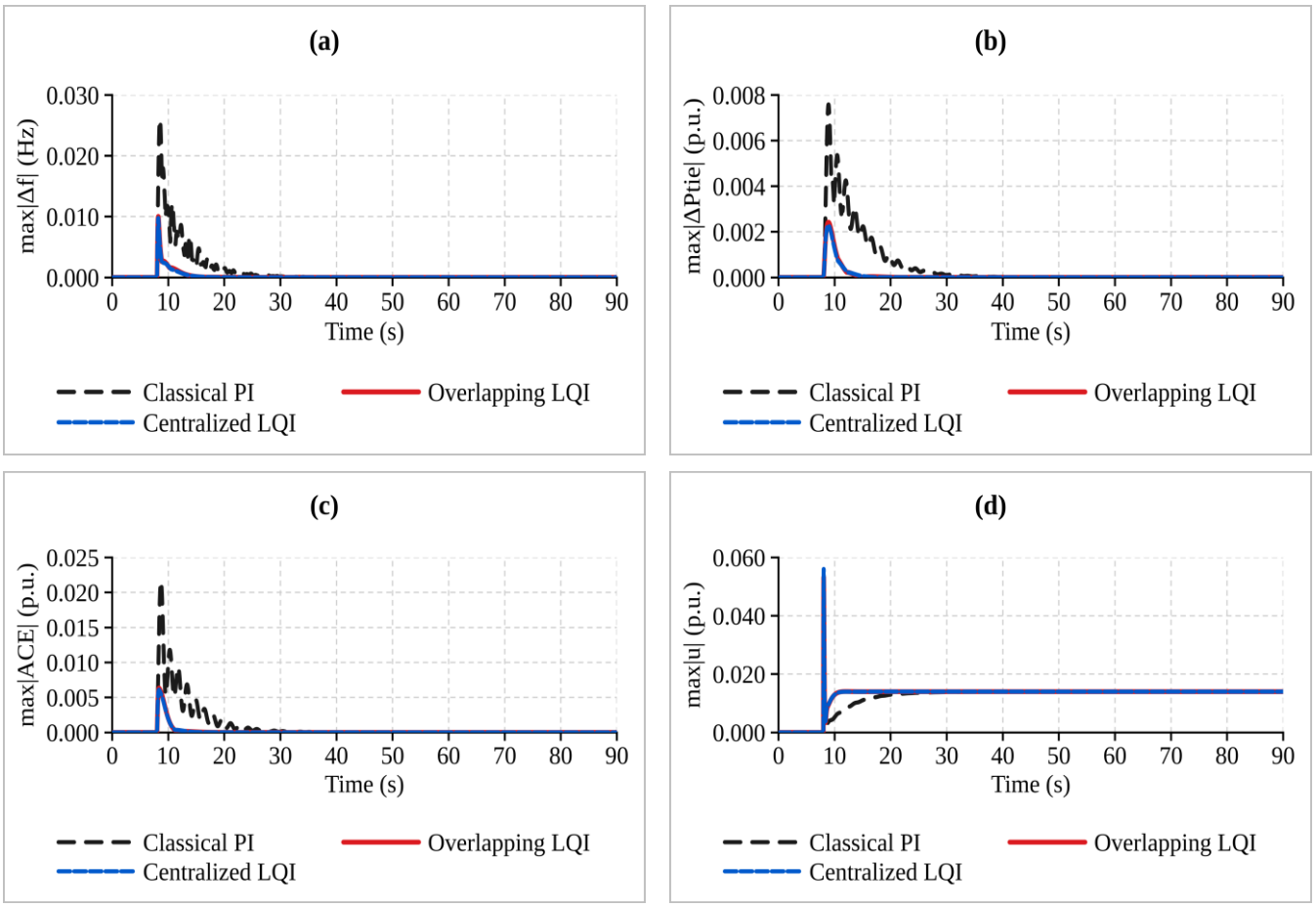

Fig. 6 Comparative responses for case 3 with coordinated parameter changes: (a) Maximum absolute frequency deviation, (b) Maximum absolute tie-line power deviation, (c) Maximum absolute ACE, and (d) Maximum absolute AGC command; curves show the maximum absolute value over the areas, with exact peaks retained.

7.4. Case 3: Coordinated Parameter Variation

As shown in Figures 6 and 7, the fixed centralized and overlapping gains are stable at the selected off-nominal point with spectral abscissae -0.503078 and -0.419316. For the proposed method, max|Δf| = 0.010018 Hz, max|ΔPtie| = 0.002421 p.u., IAE = 0.024533 and Ts = 7.48 s.

The indices are improved by 61.47%, 68.07%, 85.93% and 69.69% compared with PI. The peak frequency and IAE are 2.63% and 4.17% higher than those of the centralized LQI, and the settling time is 6.57% shorter. This single point illustrates the sensitivity of the responses; robustness over an uncertainty region is assessed in Section 7.6.

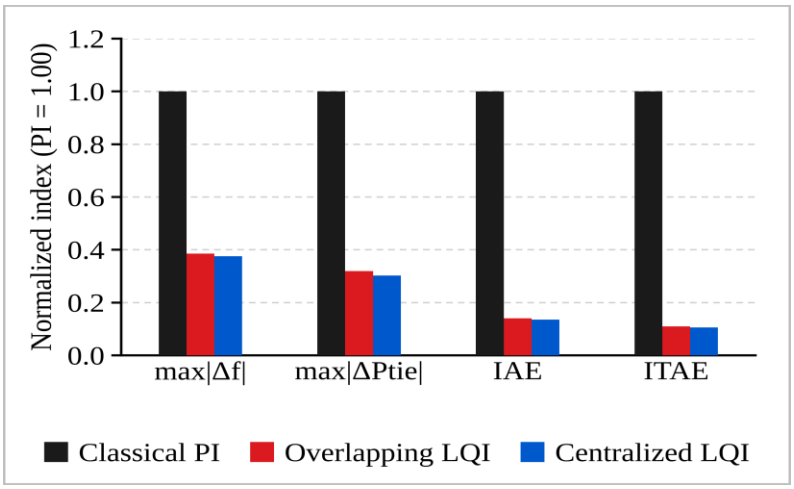

Fig. 7 PI-Normalized performance indices for case 3 (Classical PI = 1.00)

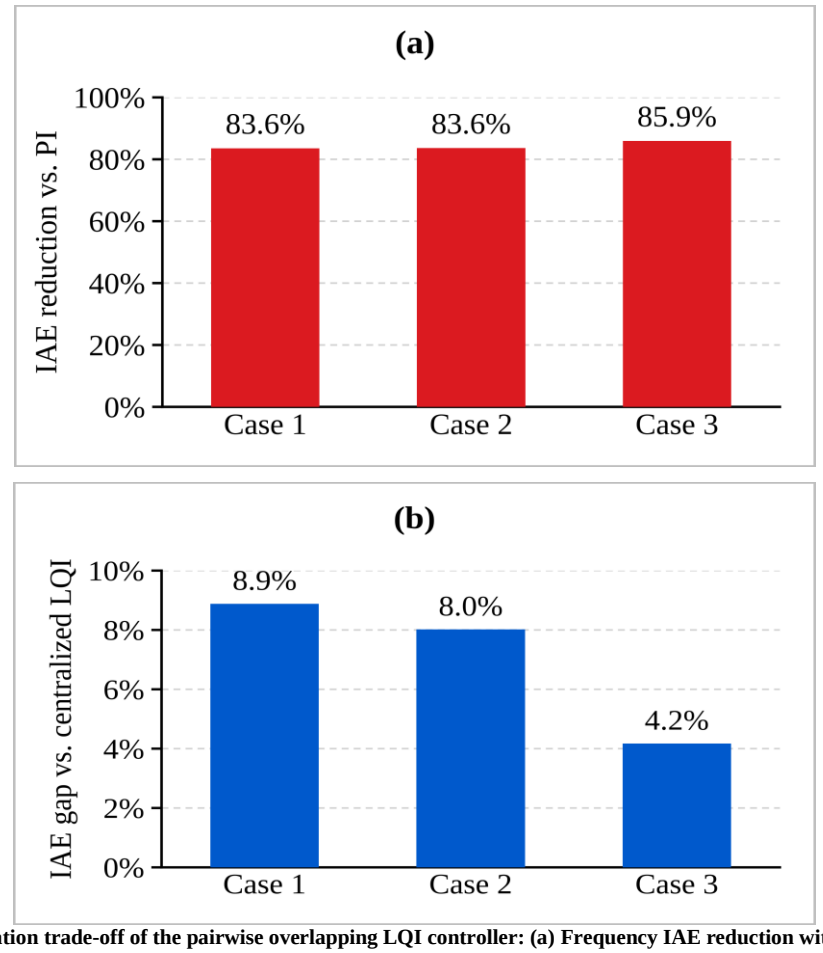

Fig. 8 Performance-Information trade-off of the pairwise overlapping LQI controller: (a) Frequency IAE reduction with respect to classical PI, and (b) residual IAE gap above centralized LQI.

As illustrated in Figure 8, the overlapping LQI controller decreases the frequency IAE by 83.6%-85.9% in the three cases compared with the classical PI control. The residual IAE gap from the centralized LQI decreases from 8.9% in Case 1 to 4.2% in Case 3, while the feedback matrix is 39.47% sparser. These results, together with the nominal cost ratio ($\rho_J = 1.179$), confirm a favorable trade-off between closed-loop performance and inter-area information requirements.

7.5. Benchmarking against Structured Controllers and Fusion Weights

Two structured benchmarks were added on the same model (Table 3). The decentralized LQI uses, in each area, a four-state LQI design on the own frequency, governor, turbine and integral states, with the tie-line flow treated as a disturbance, so it needs no communication (16 nonzero gains). The structured-optimal LQI keeps the sparsity pattern of K_{pov} and minimizes $\mathrm{tr}(P)$ for the centralized weights Q_c and R_c with a projected-gradient iteration started at K_{pov}, as in the structured design step of [24]; it represents the best gain, in this quadratic sense, that the same information pattern allows. According to Table 4, the overlapping LQI reduces the frequency IAE by 9.98%, 7.76% and 6.75% and the frequency peak by 2.00%-2.73% with respect to decentralized LQI in Cases 1-3. In Case 1 the 8.88% IAE gap to centralized LQI splits almost evenly into a pattern-related part (structured optimum 3.97% above centralized LQI) and a synthesis-related part (overlapping law 4.72% above the structured optimum); in Case 2 the two parts are 6.67% and 1.26%. In Case 3 the structured-optimal gain, which is optimized for the nominal parameters, gives a 10.2% higher IAE than the overlapping law. The decomposition-based synthesis therefore loses less than 5% of IAE with respect to the best gain with the same pattern.

Table 5 shows the effect of the fusion weights. All tested combinations give a Hurwitz closed loop with spectral abscissa between -0.396 and -0.446, and the Case 1 frequency peak (0.010456-0.010466 Hz) and peak command (0.0549 p.u.) are almost unchanged, so the weights mainly influence the slower integral modes. Among the symmetric settings, $\eta_2 = \eta_3 = 0.5$ gives the smallest worst-direction cost ratio ($\rho_J = 1.1788$) and the smallest Case 2 IAE, whereas $\eta_2 = \eta_3 = 1$ raises the ratio to 1.389. The asymmetric choice $\eta_2 = 0$, $\eta_3 = 1$, in which both interior areas follow the middle pair (2,3), gives a slightly better result ($\rho J = 1.169$ and a 1.5% lower Case 2 IAE), but makes both interior commands depend on a single pair design and a single communication link. The symmetric setting is therefore retained, and the weights are regarded as a tuning option rather than a critical parameter.

Table 5. Influence of the fusion weights on stability, cost and disturbance rejection

η_2	η_3	Spectral abscissa	ρ_J	Case 1 IAE	Case 1 max$\lvert\Delta f\rvert$ (Hz)	Case 2 IAE
0.00	0.00	-0.4192	1.2960	0.028477	0.010456	0.054710
0.25	0.25	-0.4213	1.1932	0.028726	0.010459	0.054364
0.50	0.50	-0.4208	1.1788	0.029145	0.010461	0.054198
0.75	0.75	-0.4175	1.2447	0.029720	0.010464	0.054226
1.00	1.00	-0.4117	1.3887	0.030446	0.010466	0.054488
0.00	1.00	-0.4455	1.1686	0.028334	0.010456	0.053373
1.00	0.00	-0.3957	1.5771	0.030378	0.010466	0.055593
0.50	0.25	-0.4153	1.2299	0.029156	0.010461	0.054540
0.25	0.75	-0.4331	1.1222	0.028699	0.010459	0.053726

Table 6. Robust LMI bounds and Monte Carlo robustness (500 samples per level, Case 1 disturbance, nominal gains)

Controller	$\alpha_{\max}$ from LMI (88-89)	±20%: stable	±20%: worst abscissa	±30%: stable	±30%: worst abscissa	±30%: IAE mean / p95
Classical PI	0.029	500/500	-0.0485	500/500	-0.0246	0.18195 / 0.19921
Decentralized LQI	0.400	500/500	-0.3470	500/500	-0.3332	0.03251 / 0.03465
Overlapping LQI	0.394	500/500	-0.3911	500/500	-0.3700	0.02939 / 0.03140
Structured-optimal LQI	0.383	500/500	-0.4656	500/500	-0.4331	0.02811 / 0.03008
Centralized LQI	0.388	500/500	-0.4694	500/500	-0.4362	0.02704 / 0.02897

7.6. Robustness and Practical Constraints

Table 6 summarizes the robustness results. The LMI of Equations (88) and (89) is feasible up to α = 0.394 for K_{pov}, 0.388 for K_{pc} and 0.400 for the decentralized gain, so quadratic stability is guaranteed for any combination of independent coefficient variations within about ±39%; for PI the quadratic certificate holds only up to ±2.9%, which reflects the conservatism of a single quadratic Lyapunov function. Because a single parameter point (Case 3) cannot establish robustness, 500 random parameter sets with independent uniform variations of ±20% and ±30% on Mi, Di, Ri, Tg,i, Tt,i and Te were also simulated for the Case 1 disturbance with the nominal gains. All controllers remained stable in every sample. The worst spectral abscissa of the overlapping loop was -0.391 and -0.370, and its 95th-percentile IAE (0.03055 & 0.03140) stayed below the mean IAE of decentralized LQI.

Table 7. Case 1 under communication delay, measurement noise and Generation-Rate Constraints (GRC)

Scenario (Case 1)	PI: IAE	DEC: IAE	OV: IAE	C: IAE	PI: max|Δf|	DEC: max|Δf|	OV: max|Δf|	C: max|Δf|
Nominal	0.17725	0.03238	0.02915	0.02677	0.03251	0.01075	0.01046	0.01029
Delay τ = 0.2 s	0.17725	0.03238	0.02917	0.02678	0.03251	0.01075	0.01045	0.01028
Delay τ = 0.5 s	0.17725	0.03238	0.02919	0.02680	0.03251	0.01075	0.01045	0.01028
Noise $\sigma = 1\times10^{-4}$ Hz	0.17748	0.04701	0.04434	0.04247	0.03251	0.01079	0.01051	0.01035
GRC 50%/min	0.19549	0.26599	0.35259	U	0.03920	0.03694	0.03722	U
GRC 10%/min	3.40477[a]	U	U	U	0.06606	U	U	U
GRC 10%/min, OV retuned	-	-	1.33790	-	-	-	0.06180	-

A sustained bounded oscillation; U: growing oscillation ending at the ±0.20 p.u. command limit; [b] integral weight 3 instead of 300 and Rp multiplied by 10 (nominal IAE 0.29264, Ts = 49.79 s under GRC).

Table 7 reports Case 1 under practical constraints, simulated with the nonlinear model including the command limit. A transport delay τ was applied to every signal received from another area, while the tie-line flows at an area boundary are measured locally. With delays of 0.2 s and 0.5 s, the IAE of the overlapping LQI changes by less than 0.2%, and no loss of stability was found for delays up to 4 s, the largest value tested, because the inter-area entries of K_{pov} are small compared with the local entries. Zero-mean measurement noise with a standard deviation of 1×10-4 Hz on all frequency signals, updated every 0.1 s, raises the IAE of all LQI controllers by about 50% and prevents the settling band from being reached, but does not change their ranking. A Generation-Rate Constraint (GRC) has a much stronger effect. With 10%/min, a typical limit for non-reheat thermal units, all LQI designs tuned for the unconstrained linear model enter a growing oscillation that ends at the command limit, because the large integral weight demands turbine ramps that the rate limit cannot deliver; PI control also oscillates but remains bounded. At 50%/min the overlapping and decentralized laws settle again, while the centralized law still oscillates. Reducing the integral weight of the pair designs from 300 to 3 and scaling R_p by 10 restores convergence under the 10%/min limit (Ts = 49.8 s, IAE = 1.338, compared with 3.405 for PI), at the cost of a slower nominal response (IAE = 0.293). The results obtained with the original weights therefore apply to units with fast ramping capability, and GRC-aware weighting or anti-windup is required for conventional thermal units.

Table 8. Feedback sparsity, communication and computation requirements

Controller	Nonzero gains	Remote signals per sample (Areas 1-4)	Total remote signals	Communication links	Off-line Riccati problems	Online MAC per sample
Classical PI	14	0, 0, 0, 0	0	None	-	14
Decentralized LQI	16	0, 0, 0, 0	0	None	4 × (4 states)	16
Overlapping LQI	46	4, 8, 8, 4	24	3 (physical neighbors)	3 × (9 states)	46
Centralized LQI	76	14, 13, 13, 14	54	6 (all-to-all) or coordinator	1 × (19 states)	76

Feedback sparsity does not translate directly into communication savings, because the tie-line flows at an area boundary are measured locally whereas the states of other areas must be transmitted. Table 8 separates the two quantities. The overlapping law has 39.5% fewer nonzero gains than centralized LQI, but it needs 55.6% fewer remote scalar signals per sampling instant (24 versus 54) and only the three physical neighbor links instead of all-to-all exchange or a central coordinator. Online computation reduces to 46 multiply-accumulate operations per sample, compared with 76. Off-line, the three nine-state CAREs can be solved independently by the pair controllers, and their cost scales with 3·93 = 2187 instead of 193 = 6859 operations for the centralized CARE.

7.7. Communication, Computation and Scalability

Table 9. Scalability study on radial chains of N areas (same weights, η = 0.5)

N areas	Nonzero gains OV / C	Sparsity	Spectral abscissa OV / C	ρ_J	IAE OV/C (step in Area 1)	IAE OV/C (step in a central area)	IAE reduction vs. PI (Area 1)
4	46 / 76	39.5%	-0.421 / -0.503	1.179	1.089	1.047 (Area 3)	83.6%
6	74 / 174	57.5%	-0.322 / -0.395	1.304	1.094	1.070 (Area 4)	81.4%
8	102 / 312	67.3%	-0.289 / -0.207	1.313	1.088	1.112 (Area 5)	81.4%
10	130 / 490	73.5%	-0.161 / -0.127	1.336	1.093	1.134 (Area 6)	81.6%

To examine scalability beyond the four-area benchmark, chains of 6, 8 and 10 areas were built by repeating the parameters of Table 2 cyclically, with the same weights and $\eta_2 = \eta_3 = 0.5$ (Table 9). The number of nonzero gains grows linearly for the overlapping law ($14N - 10$) and quadratically for centralized LQI ($N(5N - 1)$), so the sparsity rises from 39.5% to 73.5%. For a load step in Area 1, the IAE ratio between the overlapping and centralized laws stays between 1.088 and 1.094; for a step in a central area, it grows moderately from 1.047 to 1.134, and the IAE reduction with respect to PI remains above 81%. The worst-direction cost ratio grows from 1.179 to 1.336. These results support the method for longer radial chains; meshed topologies with loops, in which the tie-line flows are not independent, are outside the scope of the present formulation.

7.8. Reasons for the Observed Performance and Comparison with Existing Approaches

Three mechanisms explain the results in Table 4 and Figures 2-8. First, the PI loop acts only on the local ACE and its integral, whereas each pairwise LQI gain feeds back the governor and turbine states of both areas in a pair together with the tie-line state that couples them. The controller therefore reacts to the generation dynamics before they appear as a frequency error, which explains the 61.5%-67.8% lower frequency peaks and the 83.6%-85.9% lower IAE values obtained with respect to PI. Second, in a chain topology, each tie-line connects exactly two neighboring areas, so the dominant dynamic coupling is already contained in the pair models. The terms not seen by the local designs are the boundary flows of non-adjacent edges and the duplication mismatch removed by convex fusion; their effect on closed-loop performance is limited, as indicated by the a posteriori cost ratio. $\rho_J = 1.179$ and by the peak-frequency gap of only 1.6%-2.6% from centralized LQI. Third, the convex fusion with $\eta_2 = \eta_3 = 0.5$ averages two locally optimal proposals for each interior area. Because both proposals are computed with the tie-line state shared by the two pairs, the averaged command does not introduce conflicting actions, and the shorter settling times observed in Cases 1 and 3 indicate that the interior areas respond in a coordinated way. With respect to the approaches reviewed in Section 2, these results agree with the general observation that a structured feedback recovers most of the centralized performance when its information pattern follows the physical coupling [18-20, 26]. Compared with fully decentralized LQR designs [27, 28], represented here by the decentralized LQI benchmark, the pairwise scheme additionally uses the states of adjacent areas and the shared tie-line state, which provides the inter-area information that a block-diagonal gain cannot exploit and lowers the IAE by 6.8%-10.0%. Compared with sparsity-promoting designs [24, 25], the information pattern is known before tuning and coincides with the tie-line graph, so the communication requirements can be specified at the planning stage; the price is that the sparsity level is not optimized and remains at 46 nonzero gains. A direct numerical comparison with the indices reported in these studies is not attempted, because they rely on different test systems, disturbances and performance definitions; the centralized LQI applied to the same model is used instead as the reference for the best performance achievable with full information.

7.9. Performance-Information Trade-Off and Limitations

Compared with centralized LQI, the peak frequency deviation of the proposed controller is 1.59%-2.63% higher, and its IAE is 4.17%-8.88% higher. In return, the feedback matrix is 39.47% sparser, the number of remote signals is 55.6% lower and one 19th-order CARE is replaced by three 9th-order CAREs, while online exchange is limited to adjacent areas. The peak command is still only 22.93%-27.45% of the assumed 0.20 p.u. bound. However, its peak control is 3.66-3.81 times that of PI, and its finite-window energy is 9.70%-10.52% higher; together with the GRC results of Section 7.6, this shows that practical deployment needs area-specific reserve, ramp-rate-aware weighting or anti-windup. Governor dead bands, renewable source dynamics, observer error, packet loss, topology switching and hardware-in-the-loop validation are not considered, and delay, noise and rate limits are examined only for Case 1. The study relies on a linearized, full-state, continuous-time model, and these limitations define the scope of the conclusions.

8. Conclusion

A pairwise overlapping LQI architecture has been developed for a four-area AGC/LFC chain based on a 19-state physical model and three nine-state pair design models (a 27-dimensional lifted space). Explicit lifting, contraction and convex-fusion maps yield a nearest-neighbor feedback law with 46 nonzero coefficients instead of the 76 required by centralized LQI, and 55.6% fewer remote signals. Exponential stability is certified by a pairwise block-diagonal Lyapunov function, and quadratic stability holds for independent coefficient variations of up to ±39%. In the three simulated cases, the proposed controller reduces the peak frequency deviation by 61.5%-67.8% and the frequency IAE by 83.6%-85.9% relative to classical PI, lowers the IAE by 6.8%-10.0% relative to decentralized LQI, and stays within 1.6%-2.6% (peak frequency) and 4.2%-8.9% (IAE) of centralized LQI. The design tolerates communication delays of up to 4 s, whereas generation-rate constraints require retuned weights. Future work should address the following issues:

- Ramp-rate-aware weighting and anti-windup for units with generation-rate constraints;
- Observer-based implementation with packet loss and measurement noise; and
- Extension to meshed topologies, real-time execution and hardware-in-the-loop validation.

Conflicts of Interest

The authors declare that there is no conflict of interest regarding the publication of this paper.

References

[1] Prabha S. Kundur, and Om P. Malik, *Power System Stability and Control*, 2nd ed., McGraw-Hill, 2025. [Google Scholar] [Publisher Link]

[2] Hassan Bevrani, *Robust Power System Frequency Control*, 1st ed., New York, Springer, 2009. [CrossRef] [Google Scholar] [Publisher Link]

[3] Ibraheem, P. Kumar, and Dwarkadas Prahladadas Kothari, "Recent Philosophies of Automatic Generation Control Strategies in Power Systems," *IEEE Transactions on Power Systems*, vol. 20, no. 1, pp. 346-357, 2005. [CrossRef] [Google Scholar] [Publisher Link]

[4] Charles E. Fosha, and Olle I. Elgerd, "The Megawatt-Frequency Control Problem: A New Approach via Optimal Control Theory," *IEEE Transactions on Power Apparatus and Systems*, vol. PAS-89, no. 4, pp. 563-577, 1970. [CrossRef] [Google Scholar] [Publisher Link]

[5] Désiré D. Rasolomampionona et al., "A Comprehensive Review of Load Frequency Control Technologies," *Energies*, vol. 17, no. 12, pp. 1-74, 2024. [CrossRef] [Google Scholar] [Publisher Link]

[6] Xin Chen, Changhong Zhao, and Na Li, "Distributed Automatic Load-Frequency Control with Optimality in Power Systems," *IEEE Transactions on Control of Network Systems*, vol. 8, no. 1, pp. 307-318, 2021. [CrossRef] [Google Scholar] [Publisher Link]

[7] Eleftherios Vlahakis, Leonidas Dritsas, and George Halikias, "Distributed LQR Design for a Class of Large-Scale Multi-Area Power Systems," *Energies*, vol. 12, no. 14, pp. 1-28, 2019. [CrossRef] [Google Scholar] [Publisher Link]

[8] Hunmin Kim, Minghui Zhu, and Jianming Lian, "Distributed Robust Adaptive Frequency Control of Power Systems with Dynamic Loads," *IEEE Transactions on Automatic Control*, vol. 65, no. 11, pp. 4887-4894, 2020. [CrossRef] [Google Scholar] [Publisher Link]

[9] Shengnan Zhang et al., "Distributed Adaptive Protocols Design-based Load Frequency Control for Multi-Area Interconnected Power System," *2021 40th Chinese Control Conference (CCC)*, pp. 6892-6897, 2021. [CrossRef] [Google Scholar] [Publisher Link]

[10] Abdullahi Bala Kunya, "Hierarchical Bi-Level Load Frequency Control for Multi-Area Interconnected Power Systems," *International Journal of Electrical Power and Energy Systems*, vol. 155, pp. 1-17, 2024. [CrossRef] [Google Scholar] [Publisher Link]

[11] Waqar Younis et al., "Robust Load Frequency Control in Renewable Integrated Multi-Area Grids using Hybrid SA and QIO Tuned PIDF Controller," *Scientific Reports*, vol. 15, no. 1, pp. 1-32, 2025. [CrossRef] [Google Scholar] [Publisher Link]

[12] Arman Oshnoei, Morteza Kheradmandi, and S.M. Muyeen, "Robust Control Scheme for Distributed Battery Energy Storage Systems in Load Frequency Control," *IEEE Transactions on Power Systems*, vol. 35, no. 6, pp. 4781-4791, 2020. [CrossRef] [Google Scholar] [Publisher Link]

[13] Yunrui Lan and Mahesh S. Illindala, "Robust Distributed Load Frequency Control for Multi-Area Power Systems with Photovoltaic and Battery Energy Storage System," *Energies*, vol. 17, no. 22, pp. 1-18, 2024. [CrossRef] [Google Scholar] [Publisher Link]

[14] Aswin N. Venkat et al., "Distributed MPC Strategies with Application to Power System Automatic Generation Control," *IEEE Transactions on Control Systems Technology*, vol. 16, no. 6, pp. 1192-1206, 2008. [CrossRef] [Google Scholar] [Publisher Link]

[15] Hassan Haes Alhelou et al., "Challenges and Opportunities of Load Frequency Control in Conventional, Modern and Future Smart Power Systems: A Comprehensive Review," *Energies*, vol. 11, no. 10, pp. 1-35, 2018. [CrossRef] [Google Scholar] [Publisher Link]

[16] M. Ikeda, D.D. Šiljak, and D.E. White, "Decentralized Control with Overlapping Information Sets," *Journal of Optimization Theory and Applications*, vol. 34, no. 2, pp. 279-310, 1981. [CrossRef] [Google Scholar] [Publisher Link]

[17] Dragoslav D. Šiljak, Large-Scale Dynamic Systems: Stability and Structure, New York, North-Holland, 1978. [Google Scholar]

[18] Xue-Bo Chen, and Srdjan S. Stanković, "Decomposition and Decentralized Control of Systems with Multi-Overlapping Structure," *Automatica*, vol. 41, no. 10, pp. 1765-1772, 2005. [CrossRef] [Google Scholar] [Publisher Link]

[19] Adel Ahmadi, and Mohammad Aldeen, "Robust Overlapping Load Frequency Output Feedback Control of Multi-Area Interconnected Power Systems," *International Journal of Electrical Power & Energy Systems*, vol. 89, pp. 156-172, 2017. [CrossRef] [Google Scholar] [Publisher Link]

[20] X.-B. Chen, and Srdjan S. Stankovic, "Overlapping Decentralized Approach to Automatic Generation Control of Multi-Area Power Systems," *International Journal of Control*, vol. 80, no. 3, pp. 386-402, 2007. [CrossRef] [Google Scholar] [Publisher Link]

[21] Qinghu Xu et al., "Research on Subsystem Division Scheme of Overlapping Decentralized Control Strategy," *Systems Science & Control Engineering*, vol. 10, no. 1, pp. 910-921, 2022. [CrossRef] [Google Scholar] [Publisher Link]

[22] Linyun Xiong, Hao Li, and Jie Wang, "LMI based Robust Load Frequency Control for Time Delayed Power System via Delay Margin Estimation," *International Journal of Electrical Power and Energy Systems*, vol. 100, pp. 91-103, 2018. [CrossRef] [Google Scholar] [Publisher Link]

[23] Lili Dong, Yao Zhang, and Zhiqiang Gao, "A Robust Decentralized Load Frequency Controller for Interconnected Power Systems," *ISA Transactions*, vol. 51, no. 3, pp. 410-419, 2012. [CrossRef] [Google Scholar] [Publisher Link]

[24] Fu Lin, Makan Fardad, and Mihailo R. Jovanović, "Design of Optimal Sparse Feedback Gains via the Alternating Direction Method of Multipliers," *IEEE Transactions on Automatic Control*, vol. 58, no. 9, pp. 2426-2431, 2013. [CrossRef] [Google Scholar] [Publisher Link]

[25] Florian Dörfler et al., "Sparsity-Promoting Optimal Wide-Area Control of Power Networks," *IEEE Transactions on Power Systems*, vol. 29, no. 5, pp. 2281-2291, 2014. [CrossRef] [Google Scholar] [Publisher Link]

[26] Lubomír Bakule, "Decentralized Control: Status and Outlook," *Annual Reviews in Control*, vol. 38, no. 1, pp. 71-80, 2014. [CrossRef] [Google Scholar] [Publisher Link]

[27] Muthana T. Alrifai, Mohamed F. Hassan, and Mohamed Zribi, "Decentralized Load Frequency Controller for a Multi-Area Interconnected Power System," *International Journal of Electrical Power and Energy Systems*, vol. 33, no. 2, pp. 198-209, 2011. [CrossRef] [Google Scholar] [Publisher Link]

[28] Ashraf M. Abdelhamid, and Ahmed A.M. El-Gaafary, "Optimal Decentralized LQR Control to Enhance Multi-Area LFC System Stability," *Mathematical Problems in Engineering*, vol. 2018, no. 1, pp. 1-11, 2018. [CrossRef] [Google Scholar] [Publisher Link]

[29] Miaomiao Ma et al., "Distributed Model Predictive Load Frequency Control of Multi-Area Interconnected Power System," *International Journal of Electrical Power and Energy Systems*, vol. 62, pp. 289-298, 2014. [CrossRef] [Google Scholar] [Publisher Link]

[30] Ch. Varaha Narasimha Raja, "Load Frequency Control in Four Area Power Systems using Fuzzy Logic PI Controller," *Bulletin of Electrical Engineering and Informatics*, vol. 2, no. 2, pp. 105-110, 2013. [CrossRef] [Google Scholar] [Publisher Link]

[31] Brian D.O. Anderson, and John B. Moore, *Optimal Control: Linear Quadratic Methods*, Prentice-Hall, 1990. [Google Scholar]

[32] Kemin Zhou, John C. Doyle, and Keith Glover, *Robust and Optimal Control*, Upper Saddle River, NJ, USA: Prentice-Hall, 1996. [Google Scholar]

[33] Sigurd Skogestad, and Ian Postlethwaite, *Multivariable Feedback Control: Analysis and Design*, Wiley, Chichester, U.K, vol. 2, 2005. [Google Scholar] [Publisher Link]

[34] Stephen Boyd et al., *Linear Matrix Inequalities in System and Control Theory*, Studies in Applied Mathematics, 1994. [Google Scholar] [Publisher Link]

Appendix

Table 10 summarizes the parameters, pair index sets, controller settings and simulation settings used in all simulations, and Table 11 lists the gain matrices of the overlapping and centralized LQI controllers.

Table 10. Simulation parameters

No.	Parameter / symbol	Values	Unit
1	Inertia constants, M	(0.1667, 0.2222, 0.1600, 0.1304)	p.u.·s/Hz
2	Load-damping coefficients, D	(0.008333, 0.008889, 0.008000, 0.008696)	p.u./Hz
3	Speed-regulation constants, R	(2.4, 2.7, 2.5, 2.0)	Hz/p.u.
4	Governor time constants, T_g	(0.080, 0.072, 0.070, 0.085)	s
5	Turbine time constants, T_t	(0.300, 0.330, 0.350, 0.375)	s
6	Frequency-bias coefficients, B_f	(0.425, 0.425, 0.425, 0.425)	p.u./Hz
7	Tie-line synchronizing coefficients, T_{12}, T_{23}, T_{34}	(0.0866, 0.0866, 0.0866)	p.u./rad
8	Pair index set, J_{12}	[1, 5, 9, 16, 2, 6, 10, 17, 13]	indices
9	Pair index set, J_{23}	[2, 6, 10, 17, 3, 7, 11, 18, 14]	indices
10	Pair index set, J_{34}	[3, 7, 11, 18, 4, 8, 12, 19, 15]	indices
11	Proportional ACE coefficient, K_P	$K_P = 0.05$	-
12	Integral coefficient, K_I	$K_I = 0.20$	-
13	AGC-command limit	$\|u_i\| \le 0.20$	p.u.
14	Integrator and step size	Fixed-step Runge-Kutta (4th order), 1 ms	-
15	Simulation horizon T_f	Case 1: 80; Cases 2 and 3: 90	s
16	Settling band for T_s	$\max_i \|\Delta f_i\| < 1\times10^{-4}$ Hz	Hz
17	Plotted data	10 ms for 12 s after each event, 0.1 s elsewhere, exact peaks kept	-
18	Riccati / Lyapunov / LMI solvers	SciPy (Schur method) / SciPy (Bartels-Stewart) / Clarabel via CVXPY	-
19	Structured-optimal gain	Projected gradient on tr(P), $\Sigma_0 = I_{19}$, start at K_{ov}, Armijo step	-

Table 11. Gain matrices of the overlapping and centralized LQI controllers (Transposed; zero entries are structural)

State	Overlapping LQI K_{ov} (rows u_1-u_4)				Centralized LQI K_c (rows u_1-u_4)			
	u_1	u_2	u_3	u_4	u_1	u_2	u_3	u_4
Δf_1	34.6772	-0.8623	0	0	34.8412	-1.3592	-0.3667	-0.1647
Δf_2	-2.0692	35.4237	-0.9979	0	-1.6344	36.8234	-1.3140	-0.4504
Δf_3	0	-0.8928	34.7074	-1.5381	-0.3757	-1.1882	35.7853	-1.1543
Δf_4	0	0	-0.7975	34.2644	-0.1637	-0.3840	-1.2281	34.4443
$\Delta P_{g,1}$	3.5778	-0.0177	0	0	3.4449	-0.0287	-0.0074	-0.0034

$\Delta P_{g,2}$	-0.0319	3.2255	-0.0158	0	-0.0258	3.1027	-0.0216	-0.0070
$\Delta P_{g,3}$	0	-0.0153	3.3601	-0.0285	-0.0065	-0.0210	3.2380	-0.0225
$\Delta P_{g,4}$	0	0	-0.0173	3.7172	-0.0036	-0.0082	-0.0273	3.5877
$\Delta P_{t,1}$	20.3746	-0.3030	0	0	20.1714	-0.4766	-0.1218	-0.0553
$\Delta P_{t,2}$	-0.6196	17.7956	-0.3044	0	-0.4859	17.9521	-0.4045	-0.1293
$\Delta P_{t,3}$	0	-0.3345	22.3004	-0.6158	-0.1352	-0.4459	22.4051	-0.4694
$\Delta P_{t,4}$	0	0	-0.3646	26.8294	-0.0714	-0.1653	-0.5626	26.5768
ΔP_{12}	15.0963	-8.9558	0	0	18.1967	-12.7290	-5.6807	-2.5103
ΔP_{23}	0	8.9611	-6.7184	0	8.1795	15.4219	-10.7012	-8.4790
ΔP_{34}	0	0	6.4414	-8.1507	2.5157	6.0603	7.6787	-11.4236
ξ_1	36.9254	0.1963	0	0	37.4152	0.3187	0.0097	-0.0023
ξ_2	-0.3925	36.9257	-0.1645	0	-0.3187	37.4144	-0.2340	-0.0741
ξ_3	0	0.1645	36.9267	-0.0823	-0.0117	0.2338	37.4158	-0.0650
ξ_4	0	0	0.0412	36.9274	0.0016	0.0746	0.0646	37.4164